

Axonal domain structure as a putative identifier of neuron-specific vulnerability to oxidative stress in cultured neurons

<https://doi.org/10.1523/ENEURO.0139-22.2022>

Cite as: eNeuro 2022; 10.1523/ENEURO.0139-22.2022

Received: 30 March 2022

Revised: 30 August 2022

Accepted: 16 September 2022

This Early Release article has been peer-reviewed and accepted, but has not been through the composition and copyediting processes. The final version may differ slightly in style or formatting and will contain links to any extended data.

Alerts: Sign up at www.eneuro.org/alerts to receive customized email alerts when the fully formatted version of this article is published.

Copyright © 2022 Burke and Trudeau

This is an open-access article distributed under the terms of the Creative Commons Attribution 4.0 International license, which permits unrestricted use, distribution and reproduction in any medium provided that the original work is properly attributed.

1 **Title Page**
2
3 1. Manuscript Title (50 word maximum):
4 **Axonal domain structure as a putative identifier of neuron-specific vulnerability to**
5 **oxidative stress in cultured neurons.**
6
7 2. Abbreviated Title (50 character maximum)
8 Axonal domain of murine PD-vulnerable neurons
9
10
11 3. List all Author Names and Affiliations in order as they would appear in the published
12 article
13 Samuel Burke(1, 2, 3) and Louis-Eric Trudeau(1,2,3)
14
15 1. Department of Pharmacology and Physiology, Faculty of Medicine, Université de
16 Montréal
17 2. Department of Neurosciences, Faculty of Medicine, Université de Montréal
18 3. Neural Signaling and Circuitry Research Group (SNC), Montréal, QC, Canada
19
20 4. Author Contributions: Each author must be identified with at least one of the following:
21 SB: Designed research, Performed research, Analyzed data, Wrote the paper.
22 LET: Designed research, Wrote the paper.
23
24 5. Correspondence should be addressed to (include email address)
25 louis-eric.trudeau@umontreal.ca
26
27 6. Number of Figures
28 8
29
30 7. Number of Tables
31 0
32
33 8. Number of Multimedia
34 0
35
36 9. Number of words for Abstract
37 251
38
39 10. Number of words for Significance Statement
40 111
41
42 11. Number of words for Introduction
43 734
44
45 12. Number of words for Discussion
46 1333
47
48 13. Acknowledgements
49 None.
50

14. Conflict of Interest A. No (State ‘Authors report no conflict of interest’) B. Yes (Please explain)

Authors report no conflict of interest’

15. Funding sources

Samuel Burke was financially supported by an FRQS doctoral training award. Louis-Eric Trudeau is financially supported by the Canadian Institutes of Health Research, the Brain Canada and Krembil Foundations, the Aligning Science Across Parkinson’s (ASAP) initiative and the Henry and Berenice Kaufmann Foundation.

Abstract

Several populations of neurons are purported to degenerate in Parkinson’s disease (PD). One current hypothesis suggests that vulnerable neurons in PD share common characteristics including projecting to voluminous territories and having extremely long and branched axonal domains with large numbers of neurotransmitter release sites. In this study, we used a mouse *in vitro* culture system to compare the axonal domain of neuronal populations suspected to be vulnerable in PD to that of neuronal populations considered at a lesser risk. In the first category, we included dopamine (DA) neurons of the substantia nigra, noradrenergic neurons of the locus coeruleus, serotonin neurons of the raphe nuclei, and cholinergic neurons of the dorsal motor nucleus of the vagus. In the second category, we included DA neurons of the ventral tegmental area, cholinergic neurons of the hypoglossal nucleus, and cholinergic interneurons of the dorsal striatum. Validating their differential vulnerability, we find that, when compared to neurons presumed to be resilient in PD, a larger proportion of neurons presumed to be vulnerable in PD degenerate in response to cell stress induced by hydrogen peroxide. We also find that they are endowed with larger axonal domains, that are more complex, have more axonal varicosities with a higher proportion of varicosities that are positive for synaptotagmin 1. Notwithstanding the obvious limitations

79 related to the dissection of small brain nuclei and to the growth of these neurons *in vitro*,
80 these findings support the hypothesis that axonal domain structure is a key characteristic of
81 neuronal vulnerability to oxidative stress.
82

83 **Significance statement**

84 Parkinson's disease (PD) causes the specific degeneration of a small number of
85 neuroanatomically and neurochemically defined neuronal populations. Current hypotheses
86 suggest that these neurons are vulnerable due to their specific physiology and morphology.
87 In this study — using mouse primary neurons — we demonstrate that, when compared to
88 neuronal populations that are suspected to be resilient in PD, neuronal populations that are
89 more vulnerable in PD are more sensitive to cell stress induced by hydrogen peroxide, and
90 that the overt length and complexity of their axonal arborizations is larger. Furthermore,
91 vulnerable neurons show a strikingly elevated proportion of axonal varicosities that are
92 positive for synaptotagmin1, suggesting that they contain more active axon terminals.

93

94

95 Introduction

96 There are no disease modifying treatments available for people living with Parkinson's
97 Disease (PD). This is clearly related to our limited understanding of why varying PD-related
98 risk factors converge in causing selective dysfunction and degeneration of several
99 neurochemically and anatomically restricted neuronal populations. A better understanding of
100 the origin of selective neuronal vulnerability in PD is therefore critical.

101

102 Canonically, PD pathology is described by the presence of Lewy bodies in the brain (for a
103 historical review see (Goedert et al., 2013)) and by the loss of neuromelanin-containing
104 dopamine (DA) neurons in the substantia nigra pars compacta (SNc). However, the
105 relationship between Lewy pathology and cell loss in PD is unclear and has not unequivocally
106 revealed why certain neurons degenerate, while others do not (Espay and Lang, 2018;
107 Surmeier et al., 2017a). Importantly, the pathology and degeneration in PD is not limited to
108 DA neurons of the SNc, but rather appears to occur in several nuclei, including the locus
109 coeruleus (Huynh et al., 2021) and pedunculopontine nucleus (Hirsch et al., 1987; Tubert et
110 al., 2019). However, more systematic stereological quantifications are clearly required to
111 confirm the nuclei showing frank cell loss and not only Lewy pathology, as well as the
112 sequence of this cell loss (Giguère et al., 2018). A better understanding of what determines
113 the vulnerability of neurons that are affected in PD is essential for progress (Surmeier et al.,
114 2017b).

115

116 An increasing amount of work supports the hypothesis that the neurons that are most
117 vulnerable in PD share distinguishing morphological and physiological characteristics – cell-
118 autonomous factors – that render them selectively vulnerable. Among these, two have been

119 increasingly gaining experimental support. The first is autonomous pacemaking, with broad
120 spikes, and high intracellular calcium oscillations (Surmeier et al., 2017b). The second is being
121 endowed with a very long, and highly branched axonal domain, with orders of magnitude
122 more neurotransmitter-release sites than most other neuron types (Pacelli et al., 2015; Parent
123 and Parent, 2006; Pissadaki and Bolam, 2013; Wong et al., 2019). It is thought that these
124 features converge in leading to elevated bioenergetic demands and an associated high level
125 of chronic oxidative stress (Pissadaki and Bolam, 2013), making the neurons less resilient to
126 mitochondrial dysfunction, proteostatic burden (Lehtonen et al., 2019) or dysfunction in
127 essential cellular systems such as the endo-lysosomal system (Vidyadhara et al., 2019).

128

129 However, two important foundations underlying this working hypothesis require additional
130 investigation. One, is the purported identity of PD-vulnerable neurons, which is still unclear
131 because comparative stereological counting of multiple nuclei in post-mortem brains from
132 PD subjects has not been achieved (Giguère et al., 2018; Lunt et al., 2021). And two, work
133 comparing cell-autonomous factors in PD-vulnerable neuronal populations has been mainly
134 limited to a comparison of SNc and VTA neurons (albeit some exceptions (Goldberg et al.,
135 2012; Sanchez-Padilla et al., 2014)).

136

137 Previous work has shown that cell-autonomous differential vulnerability of SNc and VTA DA
138 neurons is maintained *in vitro*, including a striking correlation between bioenergetic
139 demands, vulnerability to PD-relevant cell stress, and axonal arbor size (Pacelli et al., 2015).
140 In the present study we use a similar *in vitro* system to examine the characteristics and
141 vulnerability of several PD-relevant neuronal populations, with the objective to evaluate the
142 hypothesis that the outright size, complexity, and extensive number of neurotransmitter

143 release sites is linked to vulnerability. We compared neurons from regions suspected to be
144 vulnerable in PD (DA neurons of the SNc, noradrenergic neurons of the locus coeruleus (LC),
145 serotonin neurons of the raphe nuclei (R), and cholinergic neurons of the dorsal motor
146 nucleus of the vagus (DMV)), to neurons from regions classically hypothesized as more
147 resilient in PD (DA neurons of the VTA (although their vulnerability in PD is controversial
148 (Alberico et al., 2015)), cholinergic neurons of the hypoglossal nucleus (XII), and cholinergic
149 interneurons of the dorsal striatum (STR)).

150

151 We find that globally, neurons previously suspected to be vulnerable in PD are less resilient
152 to cell stress induced by hydrogen peroxide, except for cholinergic neurons of the DMV. In
153 keeping with the hypothesis of a link between axonal domain complexity and vulnerability,
154 we also find that these vulnerable neurons, on average, have longer and more complex
155 axonal domains, with a much higher proportion of varicosities containing the Ca^{2+} sensor
156 synaptotagmin 1 (Syt1) and that are thus likely active. Together these findings support the
157 notion of a link between axonal complexity and basal vulnerability of neurons in the context
158 of oxidative stress.

159 **Materials and Methods**

160 **Animals**

161 Procedures with animals and their care were conducted in accordance with the Guide to care
162 and use of Experimental Animals of the Canadian Council on Animal Care (Canadian Council
163 on Animal Care, 1993). Experimental protocols were approved by the animal ethics
164 committees of the Universite de Montreal. Housing was at a constant temperature of 21°C
165 and humidity of 60%, under a fixed 12-hour light / dark cycle, with food water available ad
166 libitum.

167

168 **Transgenic animals used**

169 All mice were maintained as heterozygotes.

170 **TH-GFP**

171 The TH-green fluorescent protein (GFP) transgenic mouse line TH-EGFP/21–31, which carries
172 the enhanced GFP gene under control of the TH promoter (Matsushita et al., 2002), was
173 maintained on a C57BL/6J background.

174

175 **DAT-Ai9**

176 Dat-Ires-Cre animals (catalog #006660, The Jackson Laboratory; (Bäckman et al., 2006)) were
177 crossed with Ai9/tdTomato mice (catalog #007905, The Jackson Laboratory; (Madisen et al.,
178 2010)), allowing conditional expression of the red fluorescent protein tdTomato in DA
179 neurons. Both of these lines are on a C57BL/6J background.

180

181 **ChAT-Ai9**

182 ChAT-IRES-Cre (catalog #006410, The Jackson Laboratory; (Rossi et al., 2011)) were crossed
183 with Ai9/tdTomato mice (catalog #007905, The Jackson Laboratory; (Madisen et al., 2010))
184 allowing conditional expression of the red fluorescent protein tdTomato in cholinergic
185 neurons. The ChAT-IRES-Cre mice are on a C57BL/6;129S6 background.

186

187 **SERT-Ai9**

188 Slc6a4-Cre (MMRRC Stock #031028-UCD; (Gong et al., 2007)) were crossed with Ai9 (catalog
189 #007905, The Jackson Laboratory; (Madisen et al., 2010)) mice, allowing conditional
190 expression of the red fluorescent protein tdTomato in serotonin neurons. The SERT-Cre mice
191 were on a C57BL/6J background.

192

193 **Primary cell culture**

194 Primary neuron cultures were prepared from dissections of male and female P0 mice as
195 described previously (Fasano et al., 2008) with slight modification: the manual dissection of
196 brain nuclei containing target neurons inevitably results in uncontrollable differences in the
197 ratio of target cells of interest to other cell types. All culture conditions were identical pre-
198 neuronal seeding, where the only difference was the target region being plated (**Figure 1A**).

199 **Figure 1B** shows the anatomical location of target structures used in this work. The
200 fluorescence of target structures was used to enable accurate dissection of target nuclei. For
201 all experiments, cells were cultured for 10 days, prior to either fixation, or live cell imaging.
202 All experiments were performed on at least 3 (3-6) independent cultures. For analysis of
203 varicosities, cultures were prepared as previously described, and seeded onto 15mm cell
204 adhesion-treated glass coverslips (65µl of 100,000 cells / ml) (Fasano et al., 2008).

205

206 **96 well plates**

207 For cell stress assays and neurite tracing, primary cultures were prepared as described above,
 208 but seeded into 96 well plates (μ -Plate 96 Well Black, ibiTreat: #1.5 polymer coverslip, tissue
 209 culture treated, sterilized; Cat.No. 89626). Since dissections of tissue surrounding targeted
 210 neurochemically and anatomically defined nuclei can vary, we pooled cells from, 3-5 post-
 211 natal day 0-2 pups, per multi well plate. This enables a reduction in, for example, total DA
 212 SNc neurons variability — culture-to-culture — even where total number of cells (neurons
 213 and glia) seeded varied. This resulted in ~ 5k to 10k cells, in total, being seeded per well. For
 214 cell stress assays, hydrogen peroxide (30% (W/W) solution, Sigma H-4381) was added at 0,
 215 100, 150, and 200 μ M, at 10 days *in vitro* (DIV), and cells were fixed at 11 DIV.

216

217 **Live cell imaging**

218 For live cell imaging, cultures were prepared as above, but seeded (200 μ l of 100,000 cells /
 219 ml) into 35mm imaging compatible glass-bottomed petri dishes (μ -Dish 35 mm, high
 220 ibiTreat: 35 mm, high wall (2 ml volume), #1.5 polymer coverslip, tissue culture treated,
 221 sterilized; Cat.No. 81156).

222

223 **Immunocytochemistry**

224 Cultures were fixed with 4% paraformaldehyde (PFA; in PBS, pH-7.4) at 10 DIV, permeabilized
 225 with 0,1% triton X-100 during 20-min, and nonspecific binding sites were blocked with 10%
 226 bovine serum albumin for 10 min. Primary antibodies were incubated overnight at room
 227 temperature: Anti-Tyrosine Hydroxylase (1:2000, AB152, Cedarlane), Anti-MAP2 (1:2000,
 228 MAB3418, Millipore Sigma), Anti-RFP (1:1000, 600-401-379, Cedarlane), Anti-Syt1 (1:200, 105
 229 102, Synaptic Systems). These were subsequently detected using Alexa Fluor-488-

230 conjugated, Alexa Fluor-546-conjugated, Alexa Fluor-568-conjugated, or Alexa Fluor-647-
231 conjugated secondary antibodies (incubated at room temperature at 1:1000 for 1 hour,
232 Invitrogen).

233

234 **Mitochondrial targeting of the ROS sensor, roGFP**

235 For all primary neuron cultures in a cre background, we expressed a MTS (mitochondrially
236 targeted sequence) form of roGFP by adding 1 μ l of AAV9-CMV-DIO-MTS-roGFP-WPRE-
237 bGHpA ($\sim 2\text{--}3 \times 10^{13}$ vector genome ml $^{-1}$ titers) to cultures at 1 DIV. For cultures targeting
238 MTS-roGFP to LC neurons, in C57 primary neurons, 1 μ l AAV9-TH-MTSroGFP ($\sim 2\text{--}3 \times 10^{13}$
239 vector genome ml $^{-1}$ titers) was used. These tools (Sanchez-Padilla et al., 2014) were kind
240 gifts from the laboratory of D James Surmeier (Department of Physiology, Feinberg School of
241 Medicine, Northwestern University, Chicago, Illinois, USA).

242

243 **Imaging & data analysis**

244 **Image acquisition**

245 Confocal imaging was carried out on an Olympus Fluoview FV1000 point-scanning confocal
246 microscope (Olympus, Tokyo, Japan). Images were scanned sequentially to prevent non-
247 specific bleed-through signal using 488, 546, and 647-nm laser excitation and a 60X (NA
248 1.42) oil immersion objective. All other imaging was acquired on a Nikon Eclipse Ti2-E
249 inverted microscope, using either a CFI Plan Apo Lambda 20X objective (for cell counting and
250 neurite tracing), or a CFI Plan Apo Lambda 60X oil immersion objective (for live cell imaging).

251

252 **Image processing and analysis, data analysis, and statistics**

253 Exploratory image visualization and analysis was done using Napari (Nicholas Sofroniew et
254 al., 2021). Subsequently, unmodified images were all processed using ImageJ (Schneider et
255 al., 2012), and custom analysis scripts written in ImageJ Macro language
256 [<https://github.com/samuelorion/burke-trudeau-2022>]).

257

258 **Raw data availability**

259 Due to the considerable volume of imaging data (> 5 TBs) generated in the present study,
260 sharing of the primary data on an open data-storage solutions was not possible. However,
261 these data are available upon request. Derived data is available at
262 (<https://github.com/samuelorion/burke-trudeau-2022>).

263

264 **Image analysis**

265 **Counts and neurite tracing**

266 To conduct unbiased and high-throughput quantifications of neuron numbers, we
267 developed our own methods to count projecting neurons. These analysis scripts can be
268 found in the associated GitHub repository. Briefly, images were processed for segmentation
269 to identify cell bodies. Segmentations were then compared to raw images and validated for
270 accuracy, where we achieved ~90% accuracy across neuron types. A slightly modified version
271 [<https://github.com/samuelorion/burke-trudeau-2022>] of the above system was adapted to
272 achieve similar performance in tracing neurites, for quantification (Figures 5 and 6).

273

274 **Reactive oxygen species quantification**

275 Imaging experiments were performed at room temperature (20–22 °C) because previous
276 studies showed that probe oxidation was nearly complete at physiological temperatures

(Sanchez–Padilla et al., 2014). Regions of interest (ROIs) were generated using an automatic segmentation approach [<https://github.com/samuelorion/burke-trudeau-2022>], where GFP positive puncta were segmented and used to measure fluorescence intensity. Recordings where a drifting baseline of more than 10% was detected – due to photobleaching or photo-oxidation of roGFP – were not included. The maximum and minimum fluorescence of mito-roGFP was determined according to a previously described procedure (Guzman et al., 2010), by application of 2 mM dithiothreitol (DTT) (to reduce the mitochondria fully), and then 100 μ M aldrithiol (Ald) (to oxidize the mitochondria fully). ROIs that did not respond to DTT and Ald were not included. The relative oxidation level was then calculated as $1 - [(F - \text{FAld})/(\text{FDTT} - \text{FAld})]$, where F represents fluorescence intensity at baseline, FDTT, F in the presence of DTT, and FAld, F in the presence of ALD. Image alignment was done using the ImageJ plugin StackReg (Thévenaz et al., 1998). For quantifications of inter-mitochondrial distances, the distance between roGFP positive puncta was manually measured using Napari. Mitochondria in the STD were not quantified due to the very high density of mitochondria, making this quantification unfeasible.

293 **Varicosities**

294 Confocal images were processed [<https://github.com/samuelorion/burke-trudeau-2022>] and
 295 varicosities were segmented. Varicosities were defined as enlargements along thin neurites
 296 with a measured width between 0.2–1 μ m, and a length of 0.3–0.5 μ m. Segmentations were
 297 then mapped onto images of Syt1 immunofluorescence signal and fluorescence intensity
 298 was quantified. To determine the status of Syt1 positivity (Figure 7A; Figure 8B), we
 299 estimated the intensity of syt1 signal in segmentations that were excluded and used this
 300 value as a cut off for Syt1 positive status.

301

302 **Statistics**

303 Given previous work in our group quantifying neuron numbers on coverslips, we conducted
 304 an a priori power analysis to detect an effect size of 25%, with a power of 80%, and an alpha
 305 = 0.05, concluding our requirement for n to be 22 for survival assays. We therefore aimed for
 306 this. However, for some wells, images were excluded due to contamination. For all other
 307 experiments, we aimed to have an n of at least 12. For statistical analyses and data
 308 visualization we used R (R Core Team, 2017), and the subsequent packages for all statistical
 309 analyses, and data visualisation (*Data Analysis Using Bootstrap-Coupled Estimation [R*
 310 *Package Dabestr Version 0.3.0]*, 2020; *RStudio | Open Source & Professional Software for*
 311 *Data Science Teams*, n.d.; *Simple Fisheries Stock Assessment Methods [r Package Fsa Version*
 312 *0.8.32]*, 2021; Müller, 2020; Pedersen, 2021; Slowikowski, 2021; Wickham, 2021, 2021; Wilke,
 313 2021). For each statistical analysis, we evaluated whether the data were parametric or non-
 314 parametric, and subsequently conducted appropriate analyses, including appropriate post-
 315 hoc multiple comparisons: described in the available supplementary .Rmd file
 316 (<https://github.com/samuelorion/burke-trudeau-2022>). In figures, we include an asterisk to
 317 indicate that, for an alpha = 0.05, there is a significant difference compared to the value for
 318 the SNc (our reference neuronal population). All other post-hoc comparisons can be found in
 319 the extended data tables. All figures include box and whiskers plots, in the style of Tukey,
 320 where we indicate the median value, and the lower and upper hinges correspond to the first
 321 and third quartiles (the 25th and 75th percentiles), and the whiskers extend to the largest
 322 and smallest value (no further than 1.5 times the interquartile range). Furthermore, where
 323 appropriate, we include individual data points. Following null hypothesis testing, we also
 324 performed estimation based on confidence intervals using the R package *dabestr* (Ho et al.,

2019). For all experiments, we conducted shared control Cumming plots, compared to the
SNc. These Cumming plots have been placed below plots, below null hypothesis testing.
Furthermore, analyses were conducted comparing neurons considered vulnerable in PD to
neurons considered more resilient in PD, where Gardner-Altman two-group estimation plots
are plotted next to main box and whisker plots.

330 Results

331 We used a mouse primary culture system in which neurons from multiple brain PD-relevant
332 regions were grown on supporting astrocytes (**Figure 1B**). These were subsequently
333 neurochemically defined, identifying them either by immunocytochemistry for their
334 neurochemical identity, or the presence of the fluorescent reporter protein TdTomato,
335 expressed in a cre-dependent manner. For this study, we chose four nuclei that are
336 considered vulnerable in PD, including DA neurons of the SNc, noradrenergic neurons of the
337 LC, serotonin neurons of the raphe nuclei, and cholinergic (ChAT+) neurons of the dorsal
338 motor nucleus of the vagus (DMV). We compared these to neuronal populations considered
339 more resilient in PD, including DA neurons of the VTA, cholinergic neurons of the
340 hypoglossal nucleus (XII), and cholinergic interneurons of the dorsal striatum (STR).

341

342 Neuronal populations considered vulnerable in PD are less resilient to cell stress induced by 343 hydrogen peroxide

344 Previous work has shown that in line with *in vivo* observations, DA neurons of the SNc *in*
345 *vitro* are more vulnerable than DA neurons of the VTA to cell stress induced by several PD-
346 relevant stressors (Lieberman et al., 2017; Pacelli et al., 2015). Here we extended such a
347 comparative analysis of neuronal vulnerability in a much larger set of neuronal populations
348 with distinct neurochemical identities. Considering the well-established contribution of
349 oxidative stress to PD pathophysiology, we compared the survival of neurons exposed to
350 three concentrations of hydrogen peroxide (100, 150 and 200 μ M), a cell stressor that is
351 expected to act on all types of neurons (**Figure 2**). A quantification of neurochemically-
352 defined neurons in these cultures revealed that, considered as a group, neurons from
353 “vulnerable” nuclei (SNc, LC, Raphe, DMV) were more sensitive to hydrogen peroxide

354 compared to neurons from “resilient” nuclei (VTA, XII, STR (Figure 2B and **Extended Table 2–**
 355 **1**).

356 A closer examination of the relative vulnerability of each neuronal population across the
 357 increasing doses of hydrogen peroxide (**Figure 3**) revealed significant effects of hydrogen
 358 peroxide at doses of 100, 150, and 200 μ M (**Extended Tables 3-1**). Notably, at 150 μ M
 359 hydrogen peroxide, cholinergic neurons of the DMV, hypoglossal nucleus and striatum
 360 showed less neuronal loss compared to SNc DA neurons, ChAT+ neurons of the DMV
 361 (unpaired mean difference of DMV (n = 16) minus SNc (n = 20) 0.197 [95CI 0.0662; 0.34]),
 362 ChAT+ neurons of the XII (Unpaired mean difference of XII (n = 23) minus SNc (n = 20) 0.152
 363 [95CI -0.0443; 0.388]), and ChAT+ neurons of the STR (Unpaired mean difference of STR (n =
 364 12) minus SNc (n = 20) 0.581 [95CI 0.35; 0.831]. In comparison, LC and Raphe neurons
 365 showed cell loss comparable to SNc DA neurons. VTA DA neurons also showed a tendency
 366 for reduced cell loss compared to SNc DA neurons, although this did not reach significance
 367 (**Figure 3**). This differential vulnerability to hydrogen peroxide persisted at 200 μ M, with VTA
 368 DA neurons and all cholinergic groups showing reduced vulnerability (**Figure 3**). Except for
 369 the DMV — hypothesized to be vulnerable in PD — our findings are in keeping with the
 370 hypothesis that in addition to DA neurons of the SNc, noradrenergic LC neurons and
 371 serotonergic Raphe neurons show elevated intrinsic vulnerability.

372

373 **No overt difference in mitochondrial ROS production is observed between neurons.**

374 The origin of the elevated vulnerability of SNc and other vulnerable neurons in PD has been
 375 previously hypothesized to result at least in part from their particularly elevated bioenergetic
 376 demands, leading to higher rates of mitochondrial oxidative phosphorylation and chronically
 377 elevated levels of oxidative stress (Bolam and Pissadaki, 2012; Pacelli et al., 2015). We

378 therefore examined basal mitochondrially-derived ROS production using the ROS sensitive
379 GFP probe, mito-roGFP. The construct was expressed in neurons using a Cre recombinase-
380 dependent AAV vector or a TH promotor (for LC neurons) (**Figure 4A**). The selective
381 expression of mito-roGFP was validated by confirming that expression was limited to
382 tdTomato-expressing neurons or to neurons positive for TH (for LC neurons, see (Extended
383 **Figure 4-1**, panel A)). Experiments were conducted by live time-lapse imaging of baseline
384 mito-roGFP fluorescence, followed by a determination of the dynamic range of the reporter
385 by measuring the fluorescence increase induced by the reducing agent DTT and the
386 fluorescence decrease induced by the oxidant molecule aldrithiol (ALD) (**Figure 4B**). The
387 signal was quantified both in the neurons' somatodendritic domain and in the neurons'
388 axonal fields (**Figure 4A**). Among the neurons examined, a broad range of basal oxidant
389 levels were identified, with some mitochondria within neurons showing low basal oxidation
390 and others showing high basal oxidation (**Figure 4C**). These experiments revealed that,
391 contrary to expectation, only ChAT+ DMV neurons had significantly reduced relative
392 oxidation, when compared to the DA SNc neurons (**Figure 4C**, **Extended Tables 4-1**).
393 Furthermore, intermitochondrial distances within the axonal domain were comparable across
394 neuron types, with a mean of $\sim 13\mu\text{m}$ (SD of 5.4) (**Figure 4D**, **Extended Table 4-2**).

395

396 **Neuronal populations considered vulnerable in PD have large axonal domains, which are**
397 **more complex than neurons considered as more resilient**

398 Previous work has shown that murine DA SNc neurons have larger and more complex axonal
399 arbors compared to VTA DA neurons, both *in vitro* (Pacelli et al., 2015), and *in vivo* (Giguère
400 et al., 2019). This observation is in line with the hypothesis that the total length and

401 complexity of the axonal domain is a cell-autonomous feature that contributes to rendering
 402 these cells most vulnerable because of its associated bioenergetic burden. Here, given our
 403 working hypothesis, we examined the morphology of the axonal domain of each neuronal
 404 population. Given the number of neuron sub-types evaluated in this study, we developed
 405 simple and robust methods to quantify the axonal domain of these projecting neurons — all
 406 quantifications normalized to the number of neurons within each well (**Figure 5A, 5B, 6A**).
 407 Given that the majority of neurites detected in these neurons were MAP-2 negative, and thus
 408 not dendrites, we considered the neurons' somatodendritic domain as being negligible in
 409 size compared to the axonal domain (**Figure 5A**) and therefore quantified neurite length as a
 410 proxy for axonal length. We find that there is a significant difference in mean total neurite
 411 length when comparing vulnerable to resilient neurons (**Figure 6B, Extended Tables 6-1**).
 412 Surprisingly, only VTA DA neurons were significantly different compared to SNc DA neurons
 413 in terms of mean neurite length per neuron (Unpaired mean difference of VTA (n = 22)
 414 minus SNc (n = 21) -9450 [95CI -16900; -5080]). However, using data analysis with bootstrap
 415 estimation suggests that both hypoglossal and striatal cholinergic neurons also have, on
 416 average, shorter axonal arborizations (Unpaired mean difference of XII (n = 19) minus SNc (n
 417 = 21) -6940 [95CI -15300; -1850], Unpaired mean difference of STR (n = 14) minus SNc (n =
 418 21) -5660 [95CI -13700; -190]. We also estimated axonal arbor complexity by measuring the
 419 total number of segmentations and average length of segmentations (**Figure 6C, 6D**).
 420 Vulnerable neurons had far more segmentations per neuron compared to resilient neurons.
 421 We find that, compared to SNc DA neurons, VTA DA neurons and hypoglossal neurons have
 422 substantially fewer segmentations per neuron (**Figure 6C, Extended Tables 6-1**). We finally
 423 estimated the average axon branch length, and no overt difference were observed between
 424 vulnerable and resilient neurons. However, VTA DA neurons, LC noradrenergic neurons, DMV

425 cholinergic neurons and hypoglossal cholinergic neurons had longer segmented neurite
426 length compared to SNc DA neurons (**Figure 6D**, Extended **Tables 6-1**) (Unpaired mean
427 difference of VTA (n = 22) minus SNc (n = 21) 64.6 [95CI -31.4; 99.1], Unpaired mean
428 difference of DMV (n = 30) minus SNc (n = 21) 77.3 [95CI -50.9; 104]). Together these results
429 suggest that even though inconsistencies were observed, globally, mean total neurite length
430 is smaller in neuronal populations suspected to be more resilient in PD and the total number
431 of neurites is also smaller in these neurons.

432

433 **Neuronal populations considered vulnerable in PD have a higher proportion of varicosities**
434 **that are positive for Syt1.**

435 Neurotransmitter release sites are known to represent sites of high energy consumption in
436 neurons (Pulido and Ryan, 2021). As such, we hypothesize that their density could represent
437 a defining characteristic of vulnerable neurons in PD. We therefore estimated the density of
438 potential neurotransmitter release sites (varicosities) along the axonal domains of these
439 projecting neurons (**Figure 7A, 7B**). Following 10 DIV, we segmented probable varicosities,
440 identified them based on morphology and dimensions, and evaluated the presence of
441 synaptotagmin1 (Syt1), a calcium sensor of exocytosis that is critical for neurotransmitter
442 release in DA neurons (Banerjee et al., 2020; Delignat-Lavaud et al., 2021; Mendez et al.,
443 2011), as an index of release-competent terminals. Strikingly, we find that vulnerable neurons
444 have a significantly higher proportion of varicosities that are positive for Syt1 (**Figure 8A, 8B**,
445 **Extended Tables 8-1**), suggesting that these neurons have a higher proportion of active
446 neurotransmitter release sites. Further examination of axonal varicosity density, calculated as
447 inter-varicosity distance and density per unit length of axon, revealed that there were no
448 major differences between vulnerable and resilient neurons, with an inter-varicose distance

449 in the range ~2-4 μ m (**Figure 8C**). Raphe serotonin and hypoglossal cholinergic neurons
450 nonetheless had slightly higher inter-varicose distances, while DMV and hypoglossal
451 cholinergic neurons had a higher density of varicosities per unit length (**Figure 8C, 8D**).
452 (Unpaired mean difference of DMV (n = 12) minus SNc (n = 12) 45.6 [95CI 34.2; 72.2]) and XII
453 neurons (Unpaired mean difference of XII (n = 12) minus SNc (n = 12) 33.2 [95CI 24.8; 47.4]).
454 Together, these results provide support for the hypothesis that a distinguishing feature of
455 vulnerable neurons is having an axonal arbor endowed with a high proportion of active
456 neurotransmitter release sites, presumably linked with higher bioenergetic requirements,
457 placing a larger load on the neuron's mitochondrial network, that is equally dense across
458 neuron types (**Figure 4D**).
459

460 Discussion

461 To our knowledge, this is the first study to compare the intrinsic vulnerability and
462 morphological characteristics of several neuronal populations suspected to be vulnerable in
463 PD, to others considered as more resilient in this disorder. The results of this study show that
464 neuronal populations considered vulnerable in PD , except for cholinergic DMV neurons, are
465 more vulnerable to oxidative stress induced by hydrogen peroxide: a cellular stress model
466 that is relevant in the context of the large body of work linking oxidative stress to cell loss in
467 PD (El Kodsí et al., 2020; Jenner, 2003; Monzani et al., 2019). We also find that vulnerable
468 neurons are endowed with a broad axonal arbor that bears a higher proportion of syt1-
469 positive axonal varicosities. Broadly, our work supports a model proposing that a large and
470 highly arborized axonal domain, coupled with a dense network of active neurotransmitter
471 release sites render projection neuromodulatory neurons vulnerable due to such
472 characteristics being linked to a high mitochondrial-dependent bioenergetic burden and
473 associated elevated sensitivity to extra-homeostatic conditions.

474 Limitations

475 Some limitations of the present study need to be considered. We compared the growth of
476 neurons obtained from different transgenic lines and expressing different fluorescent
477 reporter proteins (GFP or TdTomato), which could possibly have influenced the vulnerability
478 of the neurons examined. The growth of the different types of neurons examined under
479 identical *in vitro* growth conditions and culture medium could have led to sub-optimal
480 growth for some of the neuronal populations, thus possibly influencing their intrinsic
481 vulnerability and biasing the results. The dissection of some of the small nuclei examined
482 could have also been imprecise and thus included small subsets of non-relevant neurons of
483 the same neurochemical identity. However, we have previously validated our dissections of

484 small nuclei such as the VTA and SNc and our previously published confirmation of the
485 differential size of their axonal arbour *in vitro* (Pacelli et al., 2015), like it is *in vivo* (Giguère et
486 al., 2019), argues that our *in vitro* conditions were sufficient to allow at least some of the
487 neurons' intrinsic growth capacity to be maintained in culture.

488

489 **Neuronal populations considered as vulnerable in PD are more sensitive to cell stress**
490 **induced by hydrogen peroxide**

491 As hypothesised, neurons considered as more vulnerable in PD were as a class most sensitive
492 to the hydrogen peroxide cell stress assay. This finding, and in particular the differential
493 vulnerability of SNc and VTA DA neurons, is in line with previous work (Mosharov et al.,
494 2009; Pacelli et al., 2015) demonstrating increased vulnerability of SNc DA neurons to both
495 hydrogen peroxide and the mitochondrial toxin MPP+. The finding that cholinergic DMV
496 neurons were relatively resilient to our neurotoxicity assay is somewhat surprising
497 considering previous data suggesting that these neurons are affected in PD. However, it is
498 also possible that DMV neurons are vulnerable in PD via mechanisms that are not directly
499 related to oxidative stress, such as through α -synuclein-dependent mechanisms (Chiu et al.,
500 2021). However, given the very limited data derived from stereological counting methods
501 validating whether DMV cholinergic neurons do, in fact, degenerate in PD (Giguère et al.,
502 2018), it remains possible that our observation is explained by the fact that DMV cholinergic
503 neurons are not particularly vulnerable in PD (Kalaitzakis et al., 2008). To strengthen these
504 assertions, within the context of this experimental paradigm, it may be pertinent in future
505 work to use other cellular stress assays, such as α -synuclein overexpression and/or α -
506 synuclein fibrils.

507

508 **ROS production was not significantly different across neuron types**

509 Using the mitochondrially-targeted ROS sensor mito-roGFP, we detected relatively similar
510 levels of basal ROS production across all neuron types examined. We also found a very large
511 spread of relative baseline oxidation status in the axonal and somatodendritic compartments
512 of neurons (**Figure 4C**). The lack of significant difference between neuron types may be a bit
513 surprising considering that basal ROS production has been found to be significantly higher
514 in SNc compared to VTA DA neurons both *in vitro* and *in vivo* (Guzman et al., 2010; Pacelli et
515 al., 2015; Sanchez–Padilla et al., 2014) — as well as in LC (Sanchez–Padilla et al., 2014) and
516 DMV neurons (Goldberg et al., 2012). One possibility is that *in vitro*, the lack of a sufficient
517 level of synaptic inputs severely limits the firing frequency of these neurons and thus the
518 level of metabolic activity and energy needs. Additional experiments driving neuronal firing
519 pharmacologically or optogenetically would be required to further test this hypothesis. The
520 use of a cell-wide ROS sensor such as DHE, as previously used (Pacelli et al., 2015), would
521 also help to assess ROS production deriving from other sources in addition to mitochondrial
522 activity.

523 Strikingly, we also made the observation that, in our *in vitro* system, the distance
524 between mitochondria along the axonal domain was consistent across neuron types (**Figure**
525 **4D**). This observation suggests that vulnerable neurons with highly complex axonal arbours
526 may have a density of mitochondria along their axons that is comparable to that of simpler,
527 more resilient neurons. And therefore, their higher level of vulnerability may not simply
528 derive from a higher density of mitochondria. It remains that given the differential
529 vulnerability to hydrogen peroxide detected in the present study, it can be assumed that
530 cell-autonomous developmental differences between these neurons are present in the *in*
531 *vitro* postnatal culture model used.

532

533 **The complexity and activity of the axonal domain may be a key component of what renders**
534 **a neuron vulnerable**

535 A striking observation arising from the present study is the finding that globally, the
536 neuronal populations that were most vulnerable to hydrogen peroxide neurotoxicity (SNc DA
537 neurons, Raphe serotonin neurons and LC noradrenergic neurons) were also the ones with
538 the largest axonal domain, and with the largest proportion of syt1-positive axonal
539 varicosities. These findings are in line with the hypothesis that at least in part, the elevated
540 vulnerability of long-range projection neuromodulatory neurons is linked to the very large
541 energetic requirements of their large numbers of neurotransmitter release sites found along
542 their vast axonal domain. This conclusion is compatible with the hypothesis that processes
543 occurring in axon terminals, and in particular vesicular neurotransmitter packaging, is
544 particularly costly for neurons in terms of energy requirements (Pulido and Ryan, 2021).

545

546 One relative “anomaly” in the present data set is the surprising resilience of cholinergic DMV
547 neurons, especially considering their large axonal domain and large proportion of syt1-
548 positive release sites. Perhaps, ChAT+ DMV neurons are significantly less vulnerable to
549 hydrogen peroxide as they develop less complex – albeit very long – axonal arborizations.
550 These arborization, in turn, contain far fewer varicosities per length of axon, despite having a
551 similar proportion of varicosities that are active. Although we did not verify this in the
552 present study, it can be reliably assumed that the presence of syt1 in varicosities is a reliable
553 indicator of release site functionality (Brose et al., 1992; Ducrot et al., 2021). A lower
554 proportion of syt1-positive axonal varicosities could result from several reasons, the simplest
555 of which would be a lower relative level of expression of this gene. One possibility is that

556 since DMV neurons project in large part to regions outside of the brain, the culture
557 conditions used in the present study did not allow these neurons to get sufficient access to
558 factors secreted by target cells in the peripheral nervous system and that are required to
559 maintain these neurons' excitability and normal baseline activity. Previous work has provided
560 support for the role of target cells in regulating the proportion of axonal varicosities formed
561 by SNc and VTA DA neurons (Ducrot et al., 2021). Furthermore, there is a vast literature on
562 the role of extracellular signals regulating axonal development (Bilimoria and Bonni, 2013).
563 Complementary electrophysiological recordings coupled to the use of genetically encoded
564 sensors of activity-dependent vesicular cycling would help to examine this possibility further.
565 It remains important to note that in the *in vitro* context used in the present study, all of the
566 examined long-range projection neurons nonetheless developed a very large and branched
567 axonal domain, orders of magnitude larger than most other neuron types under similar
568 conditions, supporting the hypothesis that an intrinsic developmental program drives such
569 exuberant axonal growth.

570

571 **Conclusion**

572 Taken together, the results presented provide further support for the general relevance of
573 the hypothesis that a key component of the selective vulnerability of neurons in PD (Wong et
574 al., 2019) takes its origin in the large axonal domain of long-range projection neurons. We
575 conclude that more efforts are now needed to better understand the bioenergetic challenges
576 imposed by having a highly branched axonal domain endowed with a large number of active
577 neurotransmitter release sites. In addition to the outright energetic demands imposed by
578 such an axonal domain and by the firing of these neurons (Pacelli et al., 2015), it is intriguing
579 to consider the possibility that such features may confer a massive demand on the

580 endolysosomal system where, notably 12 out of 23 PARK genes (to denote their putative link

581 to PD) are involved (Vidyadhara et al., 2019).

582

583

584

585 **Figure legends**

586

587 **Figure 1: Overview of experimental paradigm, image processing pipeline and**
588 **neuroanatomical regions and identify of target structures used for primary cultures.**

589 **A)** The brain of post-natal day 0-2 mouse pups were dissected, and target structures isolated
590 before cell dissociation and culture in 96-well plates for 10 DIV. **B)** Overview of the eight
591 target structures and subsequent dissection strategy in 4 transgenic mouse lines (TH-GFP,
592 DAT-Ai9, ChAT-Ai9, and SERT-Ai9). Additional images are from the Allen Developing Mouse
593 Brain Atlas ("ISH Data :: Allen Brain Atlas: Developing Mouse Brain," 2008; Lein et al., 2007).

594

595 **Figure 2: Vulnerable neurons are more vulnerable to hydrogen peroxide than resilient**
596 **neurons.**

597 Neurons were treated with hydrogen peroxide at 10 DIV, and fixed at 11 DIV. **A)** Example
598 photomicrographs of all positive-identified neuron types across the vulnerable, and resilient
599 target structures. **B)** Normalized number of positive neurons across hydrogen peroxide
600 concentrations. Box and whiskers plots, in the style of Tukey, where the median value is
601 indicated, and the lower and upper hinges correspond to the first and third quartiles. * =
602 one-way ANOVA, Tukey's HSD, $p < 0.05$; *= *pairwise t-test, vulnerable vs resilient, $p < 0.05$.*
603 *Detailed statistical tests and multiple comparisons can be found in Extended Data Table 2-1.*

604

605 **Figure 3: Differential vulnerability between neurons to hydrogen peroxide.**

606 Normalized number of positive-neurons, for each concentration of hydrogen peroxide, and
607 neuronal population. Box and whiskers plots, in the style of Tukey, where the median value is
608 indicated, and the lower and upper hinges correspond to the first and third quartiles,

609 Kruskal-Wallis multiple comparison, p-values adjusted with the Bonferroni method, * = $p <$
 610 0.05. Shared control estimation plot: mean difference for comparisons against the shared
 611 control, SNc, using Data Analysis with Bootstrap Estimation, with 5000 bootstrap resamples.
 612 All confidence intervals are bias-corrected and accelerated. *Detailed statistical tests and*
 613 *multiple comparisons can be found in Extended Data Tables 3–1.*

614
 615 **Figure 4: No overt difference in ROS production is observed between neurons**

616 **A)** The redox sensitive GFP, roGFP, was expressed in a cre-dependent manner in target
 617 neurons. Photomicrographs of roGFP in a TdTomato-positive SNc DA neuron, in the
 618 somatodendritic compartment (STD) and in the axonal compartment. **B)** Example traces of
 619 GFP fluorescence arbitrary units (AU) in responsive ROIs, in an SNc DA neuron. Two traces
 620 are shown: for a GFP-positive puncta that showing low relative oxidation status, and for a
 621 GFP-positive puncta showing high relative oxidation status. **C)** Quantification of the relative
 622 oxidative state of mitochondria across neuron types. Box and whiskers plots, in the style of
 623 Tukey, where the median value is indicated, and the lower and upper hinges correspond to
 624 the first and third quartiles, Kruskal-Wallis multiple comparison, p-values adjusted with the
 625 Bonferroni method, * = $p <$ 0.05. Shared control estimation plot: mean difference for
 626 comparisons against the shared control, SNc, using Data Analysis with Bootstrap Estimation,
 627 with 5000 bootstrap resamples. All confidence intervals are bias-corrected and accelerated.
 628 **D)** Quantification of inter-mitochondrial distance in the axonal domain (measured from the
 629 centre of each GFP positive puncta). Box and whiskers plots, in the style of Tukey, where the
 630 median value is indicated, and the lower and upper hinges correspond to the first and third
 631 quartiles, Kruskal-Wallis $p >$ 0.05. Density plots show distribution of individual measurements.
 632 *Detailed statistical tests and multiple comparisons can be found in Extended Data Tables 4–1*

633 and 4-2. Extended Figure 4-1 also provides micrographs showing the expression of
 634 MTSroGFP in locus coeruleus neurons and comparative data on the relative oxidation in the
 635 somatodendritic and axon domain of the different neuron types, as well as the normalized
 636 number of DAPI-positive nuclei in the neuron survival experiments performed with hydrogen
 637 peroxide.

638

639

640 **Figure 5: Overview of neurite tracing for quantification.**

641 **A)** Photomicrograph of SNc DA neurons, and overview of neurite quantification method. **B)**
 642 Photomicrographs illustrating the different types of neurons examined, with their
 643 neurochemical marker immunocytochemistry.

644

645 **Figure 6: Vulnerable neurons have large axonal domains, which are globally more complex**
 646 **than resilient neurons**

647 **A)** Overview of quantification method for neurite segmentations. **B)** Quantification of mean
 648 neurite length (total neurite length, per well, divided by number of neurons). Box and
 649 whiskers plots, in the style of Tukey, where the median value is indicated, and the lower and
 650 upper hinges correspond to the first and third quartiles, Kruskal-Wallis multiple comparison,
 651 p-values adjusted with the Bonferroni method, * = $p < 0.05$. Shared control estimation plot:
 652 mean difference for comparisons against the shared control, SNc, using Data Analysis with
 653 Bootstrap Estimation, with 5000 bootstrap resamples. All confidence intervals are bias-
 654 corrected and accelerated. **C)** Quantification of mean number of segmentations (sections) of
 655 neurites segmented per neuron. Box and whiskers plots, in the style of Tukey, where the
 656 median value is indicated, and the lower and upper hinges correspond to the first and third

657 quartiles, Kruskal-Wallis multiple comparison, p-values adjusted with the Bonferroni method,
 658 * = $p < 0.05$. Shared control estimation plot: mean difference for comparisons against the
 659 shared control, SNc, using Data Analysis with Bootstrap Estimation, with 5000 bootstrap
 660 resamples. All confidence intervals are bias-corrected and accelerated. **D)** Quantification of
 661 mean length of segmentations (sections) of neurites segmented per neuron. Box and
 662 whiskers plots, in the style of Tukey, where the median value is indicated, and the lower and
 663 upper hinges correspond to the first and third quartiles, Kruskal-Wallis multiple comparison,
 664 p-values adjusted with the Bonferroni method, * = $p < 0.05$. Shared control estimation plot:
 665 mean difference for comparisons against the shared control, SNc, using Data Analysis with
 666 Bootstrap Estimation, with 5000 bootstrap resamples. All confidence intervals are bias-
 667 corrected and accelerated. B to C have a supplementary plot of all data grouped as
 668 Vulnerable and Resilient, where an independent 2-group Mann-Whitney U Test was
 669 performed, and an asterisk denotes $p < 0.05$. Precise values can be found in the
 670 supplementary tables alongside unpaired Gardner-Altman two group estimation plots.
 671 *Detailed statistical tests and multiple comparisons can be found in Extended Data Tables 6–*
 672 *1.*

673
 674 **Figure 7: Identification of potential functional axonal varicosities by Syt1**
 675 **immunocytochemistry.**

676 **A)** Overview of the image analysis strategy used for quantification of Syt1 positivity of
 677 varicosities, and distribution of Syt1 intensity within varicosities (bottom right). **B)**
 678 Photomicrographs of axonal fields of neurons, with their neurochemical marker and Syt1
 679 immunocytochemistry.

680

681 **Figure 8: Vulnerable neurons have a higher proportion of varicosities that are positive for**
 682 **Syt1**

683 **A)** Density plot of Syt1 intensity (arbitrary units (AU) - fluorescence) in all segmented
 684 varicosities included for analysis (red line indicate quintiles). **B)** Quantification of the
 685 proportion of varicosities that are positive for Syt1. Box and whiskers plots, in the style of
 686 Tukey, where the median value is indicated, and the lower and upper hinges correspond to
 687 the first and third quartiles, Kruskal-Wallis multiple comparison, p-values adjusted with the
 688 Bonferroni method, * = $p < 0.05$. Shared control estimation plot: mean difference for
 689 comparisons against the shared control, SNC, using Data Analysis with Bootstrap Estimation,
 690 with 5000 bootstrap resamples. All confidence intervals are bias-corrected and accelerated.
 691 **C)** Quantification of inter-varicose distance (nearest neighbour analysis of segmentations).
 692 Box and whiskers plots, in the style of Tukey, where the median value is indicated, and the
 693 lower and upper hinges correspond to the first and third quartiles, Kruskal-Wallis multiple
 694 comparison, p-values adjusted with the Bonferroni method, * = $p < 0.05$. Shared control
 695 estimation plot: mean difference for comparisons against the shared control, SNC, using Data
 696 Analysis with Bootstrap Estimation, with 5000 bootstrap resamples. All confidence intervals
 697 are bias-corrected and accelerated. **D)** Mean number of varicosities per unit length of axonal
 698 domain. Box and whiskers plots, in the style of Tukey, where the median value is indicated,
 699 and the lower and upper hinges correspond to the first and third quartiles, Kruskal-Wallis
 700 multiple comparison, p-values adjusted with the Bonferroni method, * = $p < 0.05$. Shared
 701 control estimation plot: mean difference for comparisons against the shared control, SNC,
 702 using Data Analysis with Bootstrap Estimation, with 5000 bootstrap resamples. All confidence
 703 intervals are bias-corrected and accelerated. B to C have a supplementary plot of all data
 704 grouped as vulnerable and resilient, where an independent 2-group Mann-Whitney U Test

705 was performed, and an asterisk denotes $p < 0.05$. Precise values can be found in the
 706 supplementary tables alongside unpaired Gardner-Altman two group estimation plots.
 707 *Detailed statistical tests and multiple comparisons can be found in Extended Data Tables 8–*
 708 *1.*

710 **Extended Data**

711 **Figure 4-1:**

712 **A)** Expression of MTSroGFP in locus coeruleus neurons. Photomicrographs of a LC
 713 noradrenergic neuron infected with AAV9-TH-MTSroGFP. The neuron is identified by the
 714 presence of TH (red). MTSroGFP is shown in green. Nuclei, stained with DAPI are shown in
 715 blue.

716 **B)** Comparing relative oxidation in neuron types and in somatodendritic domain and axons
 717 shows only very small differences. Compared with Welch Two Sample t-test.

718 **C)** Normalized number of nuclei (DAPI positive) across hydrogen peroxide concentrations.
 719 Box and whiskers plots, in the style of Tukey, where the median value is indicated, and the
 720 lower and upper hinges correspond to the first and third quartiles. * = one-way ANOVA,
 721 Tukey's HSD, $p < 0.05$; *= *pairwise t-test, vulnerable vs resilient, $p < 0.05$.*

723 **Table 2–1:** Statistical reporting for Figure 2B

724 **Tables 3–1:** Statistical reporting for Figure 3A, 3B, 3C, 3D

725 **Tables 4–1:** Statistical reporting for Figure 4C

726 **Tables 4–2:** Statistical reporting for Figure 4D

727 **Tables 6–1:** Statistical reporting for Figure 6B, 6C, 6D

728 **Tables 8–1:** Statistical reporting for Figure 8B, 8C, 8D

731 **References**

732

733 Alberico SL, Cassell MD, Narayanan NS (2015) The Vulnerable Ventral Tegmental Area in

734 Parkinson's Disease. *Basal Ganglia* 5:51–55.

735 Banerjee A, Lee J, Nemcova P, Liu C, Kaeser PS (2020) Synaptotagmin-1 is the Ca^{2+} sensor

736 for fast striatal dopamine release. *eLife* 9.

737 Bilimoria PM, Bonni A (2013) Molecular Control of Axon Branching. *The Neuroscientist* 19:16–

738 24.

739 Bolam JP, Pissadaki EK (2012) Living on the edge with too many mouths to feed: Why

740 dopamine neurons die. *Mov Disord* 27:1478–1483.

741 Brose N, Petrenko AG, Südhof TC, Jahn R (1992) Synaptotagmin: A Calcium Sensor on the

742 Synaptic Vesicle Surface. *Science* 256:1021–1025.

743 Canadian Council on Animal Care (1993) Guide to the care and use of experimental animals.

744 Vol. 1. Vol. 1. Ottawa, Ont.: Canadian Council on Animal Care.

745 Chiu W-H, Kovacheva L, Musgrove RE, Arien-Zakay H, Koprach JB, Brotchie JM, Yaka R, Ben-

746 Zvi D, Hanani M, Roeper J, Goldberg JA (2021) α -Synuclein-induced Kv4 channelopathy in

747 mouse vagal motoneurons drives nonmotor parkinsonian symptoms. *Sci Adv* 7:eabd3994.

748 Data Analysis using Bootstrap-Coupled Estimation [R package dabestr version 0.3.0] [WWW

749 Document] (2020). URL <https://CRAN.R-project.org/package=dabestr> (accessed 6.3.21).

750 Delignat-Lavaud B, Kano J, Ducrot C, Massé I, Mukherjee S, Giguère N, Moquin L, Lévesque C,

751 Nanni SB, Bourque M-J, Rosa-Neto P, Lévesque D, Beaumont LD, Trudeau L-É (2021) The

752 calcium sensor synaptotagmin-1 is critical for phasic axonal dopamine release in the striatum

753 and mesencephalon, but is dispensable for basic motor behaviors in mice. *bioRxiv*

754 2021.09.15.460511.

755 Ducrot C, Bourque M-J, Delmas CV, Racine A-S, Guadarrama Bello D, Delignat-Lavaud B,
 756 Domenic Lycas M, Fallon A, Michaud-Tardif C, Burke Nanni S, others (2021) Dopaminergic
 757 neurons establish a distinctive axonal arbor with a majority of non-synaptic terminals. *FASEB*
 758 *J* 35:e21791.
 759 El Kods DN, Tokarew JM, Sengupta R, Lengacher NA, Ng AC, Boston H, Jiang Q, Palmberg C,
 760 Pileggi C, Shutinoski B (2020) Parkinson disease-linked parkin mediates redox reactions that
 761 lower oxidative stress in mammalian brain. *BioRxiv*.
 762 Espay AJ, Lang AE (2018) Parkinson Diseases in the 2020s and Beyond: Replacing Clinico-
 763 Pathologic Convergence With Systems Biology Divergence. *J Park Dis* 8:S59–S64.
 764 Fasano C, Thibault D, Trudeau L-É (2008) Culture of Postnatal Mesencephalic Dopamine
 765 Neurons on an Astrocyte Monolayer. *Curr Protoc Neurosci* 44:3.21.1-3.21.19.
 766 Giguère N, Burke Nanni S, Trudeau L-E (2018) On Cell Loss and Selective Vulnerability of
 767 Neuronal Populations in Parkinson's Disease. *Front Neurol* 9:455.
 768 Giguère N, Delignat-Lavaud B, Herborg F, Voisin A, Li Y, Jacquemet V, Anand-Srivastava M,
 769 Gether U, Giros B, Trudeau L-É (2019) Increased vulnerability of nigral dopamine neurons
 770 after expansion of their axonal arborization size through D2 dopamine receptor conditional
 771 knockout. *PLOS Genet* 15:e1008352.
 772 Goedert M, Spillantini MG, Del Tredici K, Braak H (2013) 100 years of Lewy pathology. *Nat*
 773 *Rev Neurol* 9:13–24.
 774 Goldberg JA, Guzman JN, Estep CM, Ilijic E, Kondapalli J, Sanchez-Padilla J, Surmeier DJ
 775 (2012) Calcium entry induces mitochondrial oxidant stress in vagal neurons at risk in
 776 Parkinson's disease. *Nat Neurosci* 15:1414–1421.

777 Gong S, Doughty M, Harbaugh CR, Cummins A, Hatten ME, Heintz N, Gerfen CR (2007)
 778 Targeting Cre recombinase to specific neuron populations with bacterial artificial
 779 chromosome constructs. *J Neurosci Off J Soc Neurosci* 27:9817–9823.
 780 Guzman JN, Sanchez-Padilla J, Wokosin D, Kondapalli J, Ilijic E, Schumacker PT, Surmeier DJ
 781 (2010) Oxidant stress evoked by pacemaking in dopaminergic neurons is attenuated by DJ-1.
 782 *Nature* 468:696–700.
 783 Hirsch EC, Graybiel AM, Duyckaerts C, Javoy-Agid F (1987) Neuronal loss in the
 784 pedunclopontine tegmental nucleus in Parkinson disease and in progressive supranuclear
 785 palsy. *Proc Natl Acad Sci* 84:5976–5980.
 786 Ho J, Tumkaya T, Aryal S, Choi H, Claridge-Chang A (2019) Moving beyond P values: data
 787 analysis with estimation graphics. *Nat Methods* 16:565–566.
 788 Huynh B, Fu Y, Kirik D, Shine JM, Halliday GM (2021) Comparison of Locus Coeruleus
 789 Pathology with Nigral and Forebrain Pathology in Parkinson’s Disease. *Mov Disord*.
 790 ISH Data :: Allen Brain Atlas: Developing Mouse Brain [WWW Document] (2008). URL
 791 <https://developingmouse.brain-map.org/> (accessed 6.4.21).
 792 Jenner P (2003) Oxidative stress in Parkinson’s disease. *Ann Neurol* 53:S26–S38.
 793 Kalaitzakis ME, Graeber MB, Gentleman SM, Pearce RKB (2008) The dorsal motor nucleus of
 794 the vagus is not an obligatory trigger site of Parkinson’s disease: a critical analysis of alpha-
 795 synuclein staging. *Neuropathol Appl Neurobiol* 34:284–295.
 796 Lehtonen Š, Sonninen T-M, Wojciechowski S, Goldsteins G, Koistinaho J (2019) Dysfunction of
 797 Cellular Proteostasis in Parkinson’s Disease. *Front Neurosci* 13.
 798 Lein ES et al. (2007) Genome-wide atlas of gene expression in the adult mouse brain. *Nature*
 799 445:168–176.

800 Lieberman OJ, Choi SJ, Kanter E, Saverchenko A, Frier MD, Fiore GM, Wu M, Kondapalli J,
 801 Zampese E, Surmeier DJ, Sulzer D, Mosharov EV (2017) α -Synuclein-Dependent Calcium
 802 Entry Underlies Differential Sensitivity of Cultured SN and VTA Dopaminergic Neurons to a
 803 Parkinsonian Neurotoxin. *eNeuro* 4:ENEURO.0167-17.2017.
 804 Lunt W, Shah M, Sang J, Choi J, Burke S, Higgins J, Skene N (2021) Neurochemical identity
 805 and anatomy of cell loss in Parkinson's disease, and the clinical data available for correlation
 806 of progression : a systematic review and meta-analysis. PROSPERO 2021.
 807 Matsushita N, Okada H, Yasoshima Y, Takahashi K, Kiuchi K, Kobayashi K (2002) Dynamics of
 808 tyrosine hydroxylase promoter activity during midbrain dopaminergic neuron development. *J*
 809 *Neurochem* 82:295–304.
 810 Mendez JA, Bourque M-J, Fasano C, Kortleven C, Trudeau L-E (2011) Somatodendritic
 811 Dopamine Release Requires Synaptotagmin 4 and 7 and the Participation of Voltage-gated
 812 Calcium Channels*. *J Biol Chem* 286:23928–23937.
 813 Monzani E, Nicolis S, Dell'Acqua S, Capucciati A, Bacchella C, Zucca FA, Mosharov EV, Sulzer
 814 D, Zecca L, Casella L (2019) Dopamine, oxidative stress and protein–quinone modifications in
 815 Parkinson's and other neurodegenerative diseases. *Angew Chem Int Ed* 58:6512–6527.
 816 Mosharov EV, Larsen KE, Kanter E, Phillips KA, Wilson K, Schmitz Y, Krantz DE, Kobayashi K,
 817 Edwards RH, Sulzer D (2009) Interplay between cytosolic dopamine, calcium, and alpha-
 818 synuclein causes selective death of substantia nigra neurons. *Neuron* 62:218–229.
 819 Müller K (2020) A Simpler Way to Find Your Files [R package here version 1.0.1] [WWW
 820 Document]. URL <https://CRAN.R-project.org/package=here> (accessed 6.3.21).
 821 Nicholas Sofroniew et al. (2021) napari/napari: 0.4.8rc2. Zenodo.

822 Pacelli C, Giguère N, Bourque M-J, Lévesque M, Slack RS, Trudeau L-É (2015) Elevated
823 Mitochondrial Bioenergetics and Axonal Arborization Size Are Key Contributors to the
824 Vulnerability of Dopamine Neurons. *Curr Biol* 25:2349–2360.
825 Parent M, Parent A (2006) Single-axon tracing study of corticostriatal projections arising from
826 primary motor cortex in primates. *J Comp Neurol* 496:202–213.
827 Pedersen TL (2021) Accelerating “ggplot2” [R package ggforce version 0.3.3] [WWW
828 Document]. URL <https://CRAN.R-project.org/package=ggforce> (accessed 6.3.21).
829 Pissadaki EK, Bolam JP (2013) The energy cost of action potential propagation in dopamine
830 neurons: clues to susceptibility in Parkinson’s disease. *Front Comput Neurosci* 7.
831 Pulido C, Ryan TA (2021) Synaptic vesicle pools are a major hidden resting metabolic burden
832 of nerve terminals. *Sci Adv* 7:eabi9027.
833 R Core Team (2017) R: A Language and Environment for Statistical Computing. Vienna,
834 Austria: R Foundation for Statistical Computing.
835 R: the r project for statistical computing [WWW Document] (n.d.). URL [https://www.r-](https://www.r-project.org/)
836 [project.org/](https://www.r-project.org/) (accessed 6.3.21).
837 Rossi J, Balthasar N, Olson D, Scott M, Berglund E, Lee CE, Choi MJ, Lauzon D, Lowell BB,
838 Elmquist JK (2011) Melanocortin-4 receptors expressed by cholinergic neurons regulate
839 energy balance and glucose homeostasis. *Cell Metab* 13:195–204.
840 RStudio | Open source & professional software for data science teams [WWW Document]
841 (n.d.). URL <https://rstudio.com/> (accessed 6.3.21).
842 Sanchez–Padilla J, Guzman JN, Ilijic E, Kondapalli J, Galtieri DJ, Yang B, Schieber S, Oertel W,
843 Wokosin D, Schumacker PT, Surmeier DJ (2014) Mitochondrial oxidant stress in locus
844 coeruleus is regulated by activity and nitric oxide synthase. *Nat Neurosci* 17:832–840.

845 Schneider CA, Rasband WS, Eliceiri KW (2012) NIH Image to ImageJ: 25 years of image
846 analysis. *Nat Methods* 9:671–675.

847 Simple fisheries stock assessment methods [r package fsa version 0. 8. 32] [WWW Document]
848 (2021). URL <https://CRAN.R-project.org/package=FSA> (accessed 6.3.21).

849 Slowikowski K (2021) Automatically Position Non-Overlapping Text Labels with “ggplot2” [R
850 package ggrepel version 0.9.1] [WWW Document]. URL [https://CRAN.R-](https://CRAN.R-project.org/package=ggrepel)
851 [project.org/package=ggrepel](https://CRAN.R-project.org/package=ggrepel) (accessed 6.3.21).

852 Surmeier DJ, Obeso JA, Halliday GM (2017a) Parkinson’s Disease Is Not Simply a Prion
853 Disorder. *J Neurosci Off J Soc Neurosci* 37:9799–9807.

854 Surmeier DJ, Obeso JA, Halliday GM (2017b) Selective neuronal vulnerability in Parkinson
855 disease. *Nat Rev Neurosci* 18:101–113.

856 Thévenaz P, Ruttimann UE, Unser M (1998) A pyramid approach to subpixel registration
857 based on intensity. *IEEE Trans Image Process Publ IEEE Signal Process Soc* 7:27–41.

858 Tubert C, Galtieri D, Surmeier DJ (2019) The pedunclopontine nucleus and Parkinson’s
859 disease. *Neurobiol Dis*, Ten years of experience of pedunclopontine nucleus deep brain
860 stimulation: A reappraisal from the basic to the clinic 128:3–8.

861 Vidyadhara DJ, Lee JE, Chandra SS (2019) Role of the endolysosomal system in Parkinson’s
862 disease. *J Neurochem* 150:487–506.

863 Wickham H (2021) Tidy Messy Data [R package tidyr version 1.1.3] [WWW Document]. URL
864 <https://CRAN.R-project.org/package=tidyr> (accessed 6.3.21).

865 Wilke CO (2021) Ridgeline Plots in “ggplot2” [R package ggrydges version 0.5.3] [WWW
866 Document]. URL <https://CRAN.R-project.org/package=ggrydges> (accessed 6.3.21).

867 Wong YC, Luk K, Purtell K, Burke Nanni S, Stoessl AJ, Trudeau L, Yue Z, Krainc D, Oertel W,
868 Obeso JA, Volpicelli-Daley LA (2019) Neuronal vulnerability in Parkinson disease: Should the
869 focus be on axons and synaptic terminals? *Mov Disord* 34:1406–1422.
870
871

Figure 1

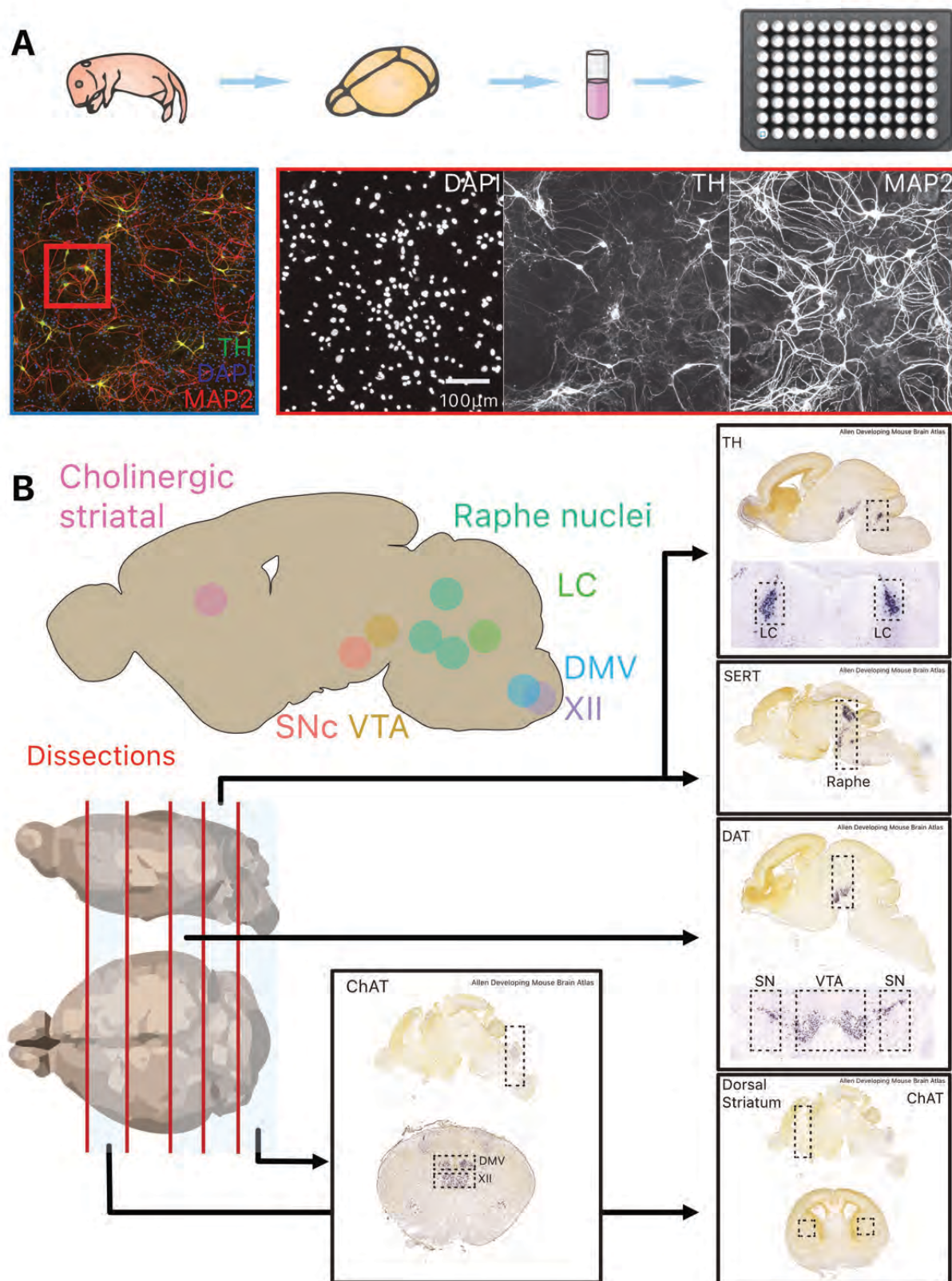


Figure 2

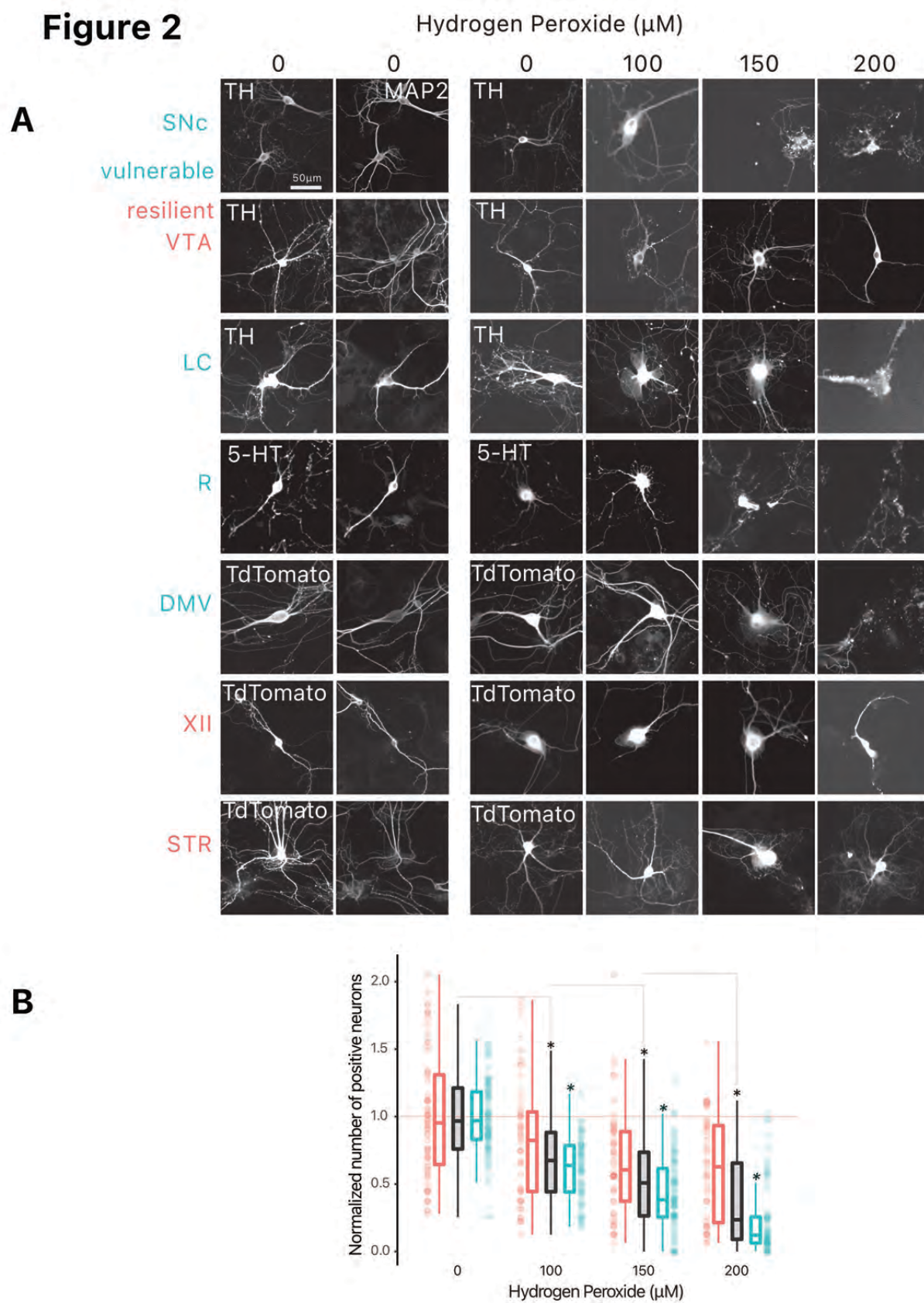


Figure 3

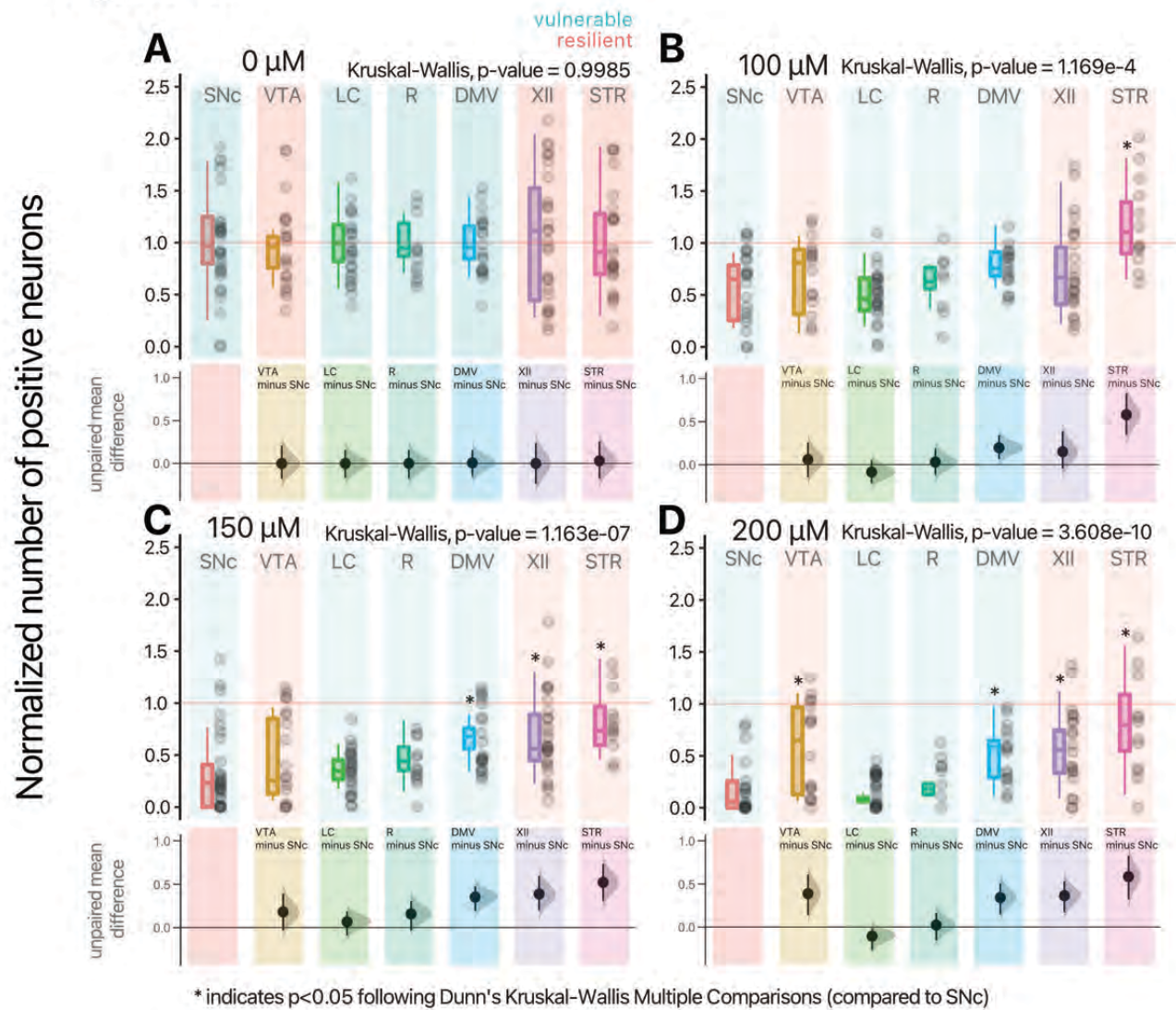


Figure 4

SNc DA neuron Somatodendritic domain

Axonal domain

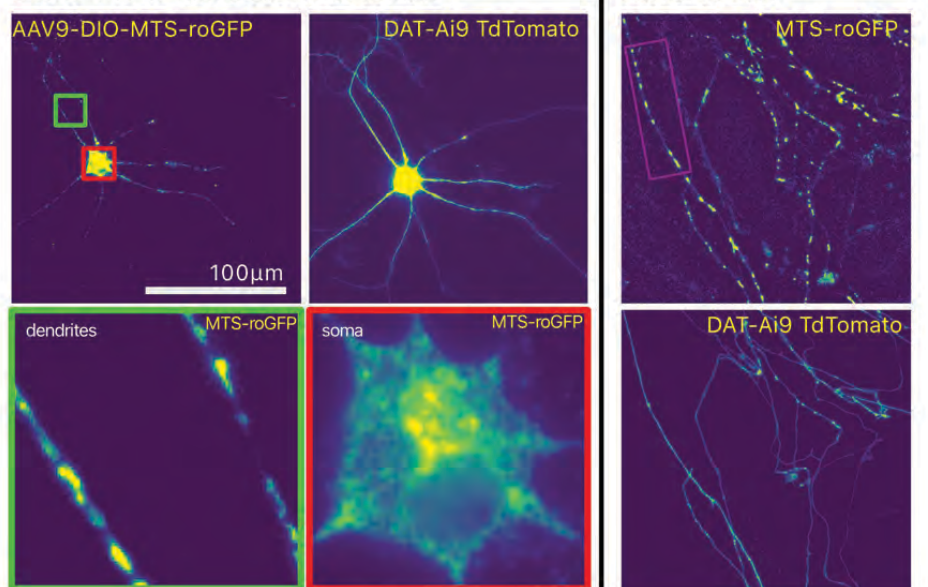
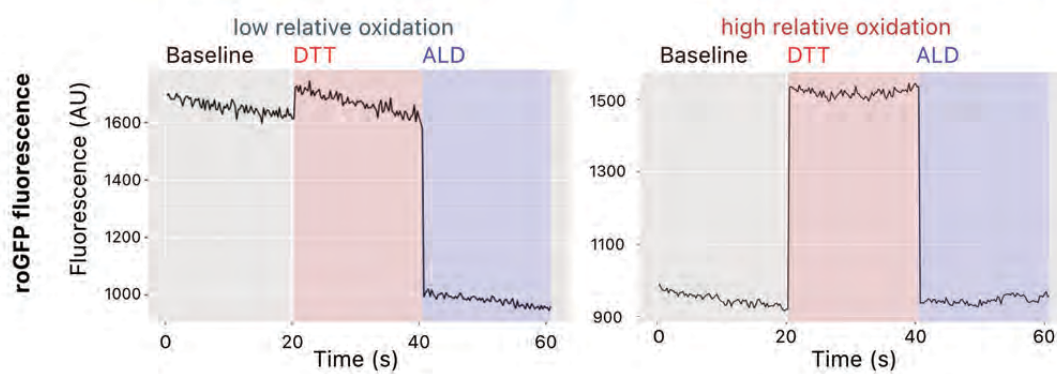
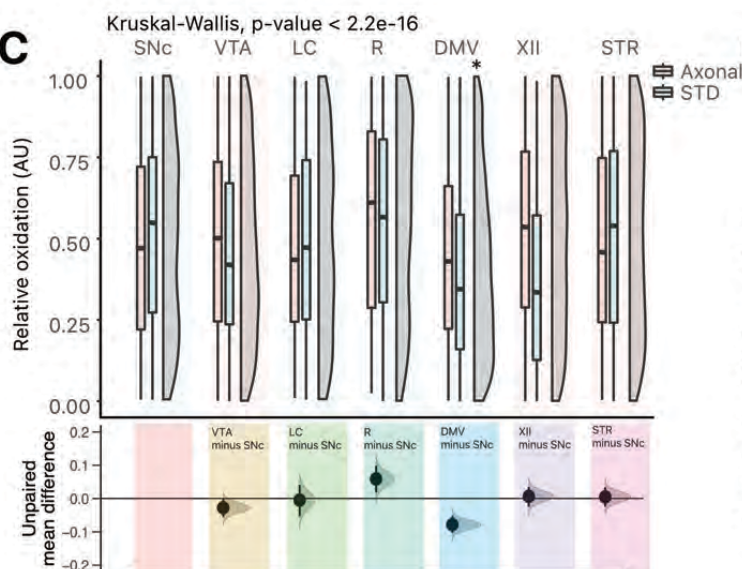
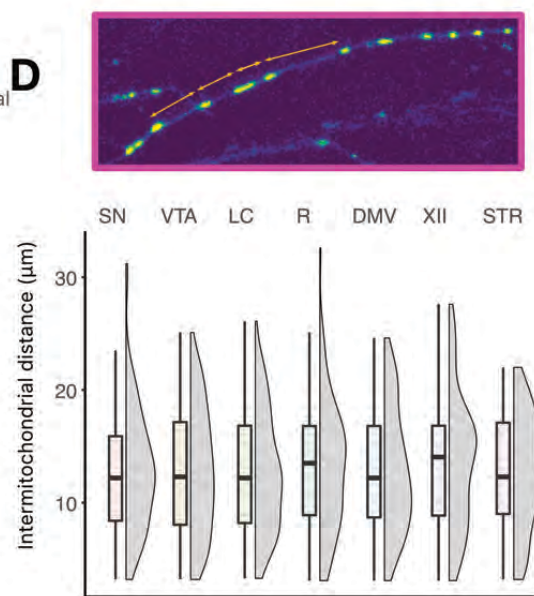
A**B****C****D**

Figure 5

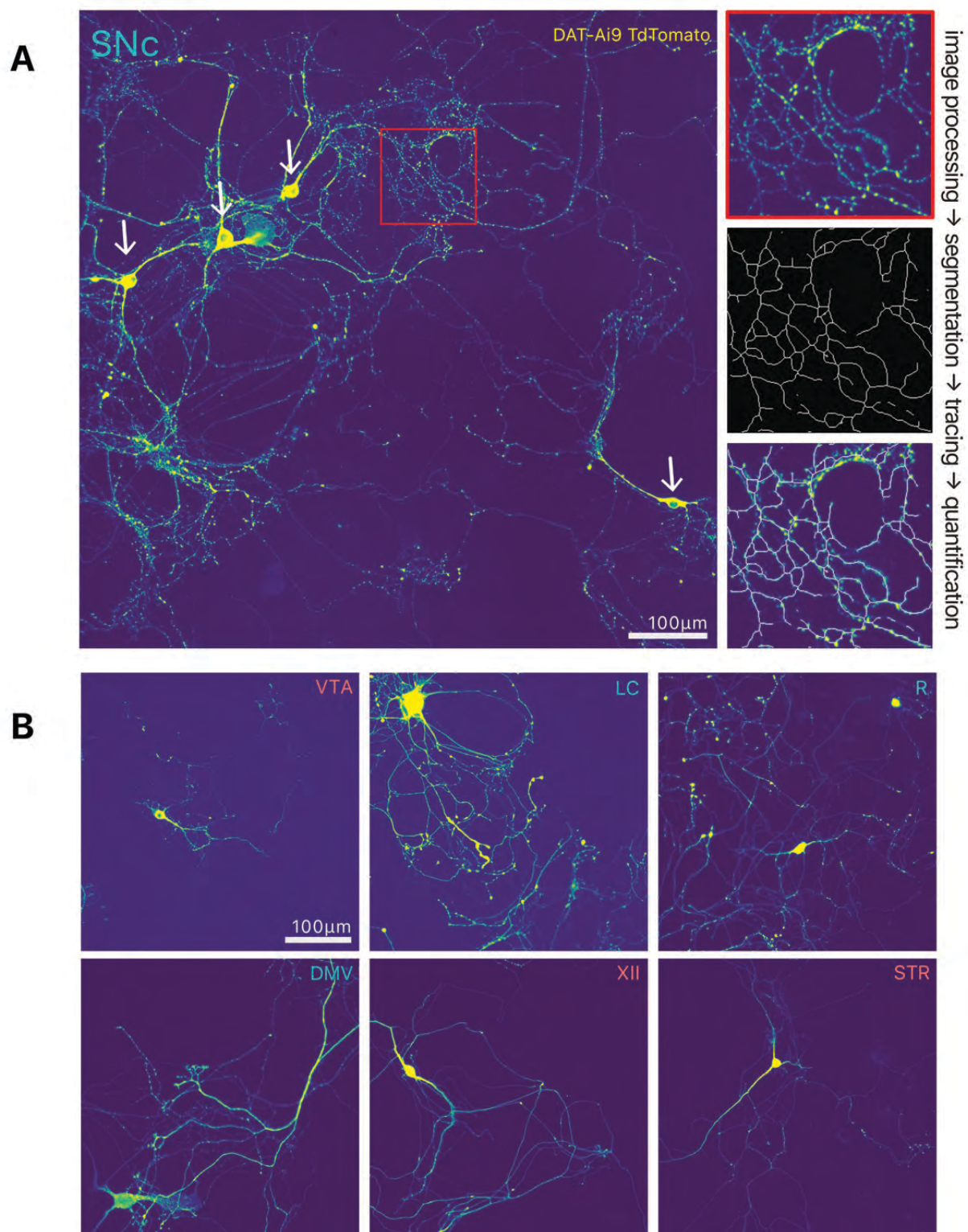


Figure 6

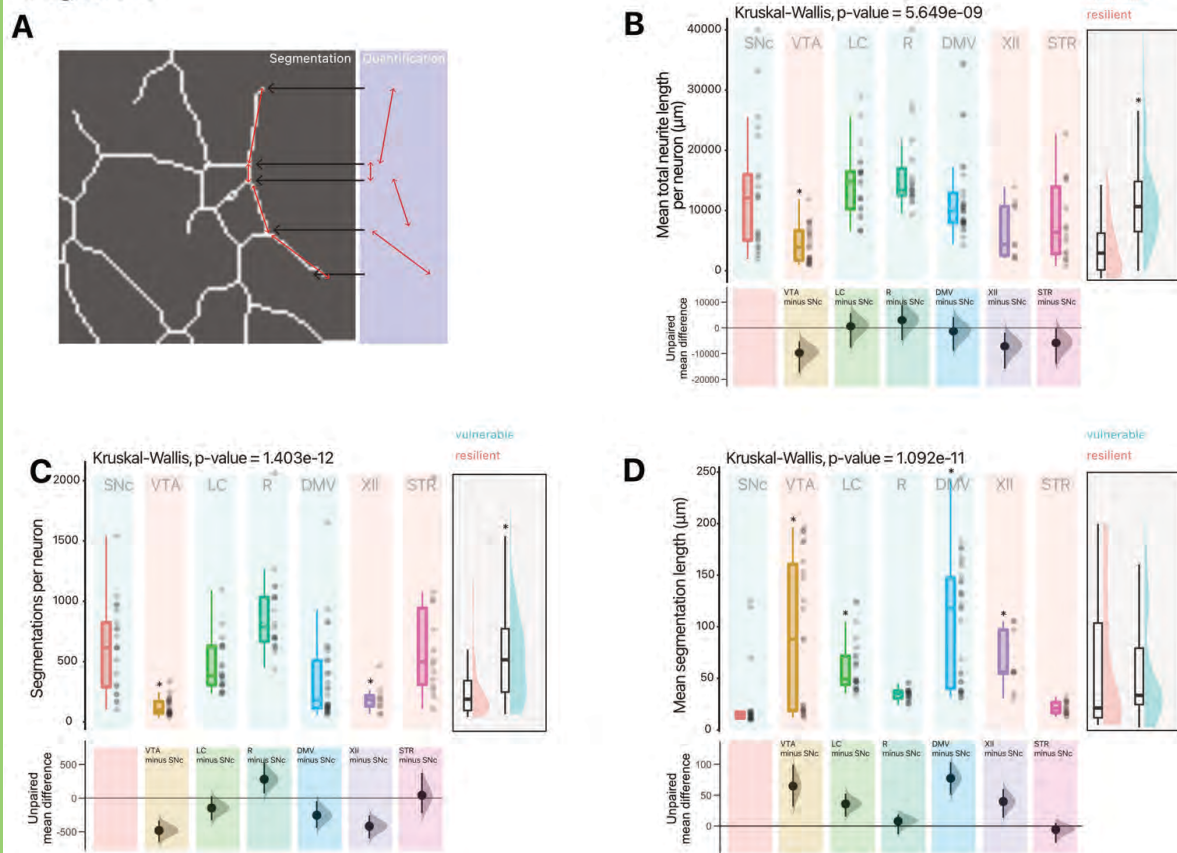


Figure 7

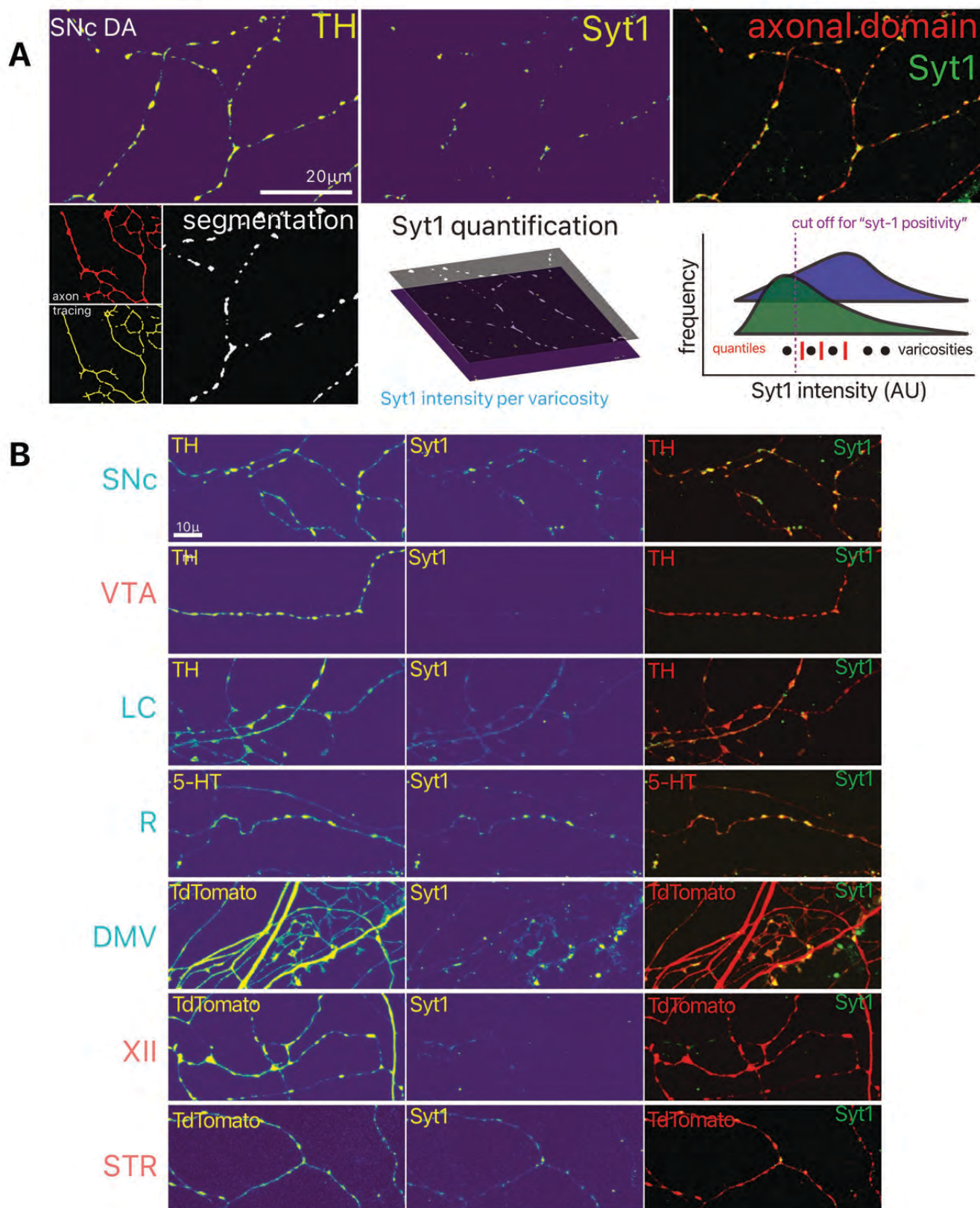


Figure 8

